Lithos 318–319 (2018) 143–157

Contents lists available at ScienceDirect

Lithos

journal homepage: www.elsevier.com/locate/lithos

Apatite: a U-Pb thermochronometer or geochronometer?

Kirkland C.L. [a,*], Yakymchuk C. [b], Szilas K. [c], Evans N. [a], Hollis J. [d], McDonald B. [a], Gardiner N.J. [a]

[a] School of Earth and Planetary Sciences (Centre for Exploration Targeting – Curtin node; John De Laeter Centre), Curtin University, Perth, WA,Australia
[b] Department of Earth and Environmental Sciences, University of Waterloo, Waterloo, ON,Canada
[c] Department of Geosciences and Natural Resource Management, University of Copenhagen, Øster Voldgade 10, Copenhagen K,Denmark
[d] Department of Geology, Ministry of Mineral Resources, Government of Greenland, PO Box 930, Nuuk, Greenland

ARTICLE INFO

Article history:
Received 29 May 2018
Accepted 3 August 2018
Available online 7 August 2018

Keywords:
Apatite
Geochronology
Themochronology
Greenland
U-Pb
Metamorphism
Pseudosection

ABSTRACT

Apatite is an accessory mineral that is frequently found in both igneous and clastic sedimentary rocks. It is conventionally considered to be characterized by a closure temperature range between 375 and 600 °C and hence has been employed to address mid-temperature thermochronology questions relevant to the reconstruction of thermal events in the middle to lower crust. However, questions remain as to whether apatite faithfully records thermally-activated volume diffusion profiles, or rather is influenced by recrystallization and new growth processes. We present a case study of two apatite samples from the Akia Terrane in Greenland that help chart some of the post magmatic history of this region. Apatite in a tonalitic gneiss has distinct U-enriched rims and its U-Pb apparent ages correlate with Mn chemistry, with a high Mn group yielding an age of c. 2813 Ma. The U-Pb and trace element chemistry and morphology support an interpretation in which these apatite crystals are originally igneous and record cooling after metamorphism, with subsequent generation of discrete new rims. Epidote observed in the sample implies a <600 °C fluid infiltration event associated with apatite rims. The second sample, from a granitic leucosome, contains apparently homogeneous apatite, however U-Pb analyses define two distinct discordia arrays with different common Pb components. An older, c. 2490 Ma, component is associated with elevated Sr, whereas a younger, c. 1800 Ma, component has lower Sr concentration. A depth profile reveals an older core with progressively younger ages towards a compositionally discrete late Paleoproterozoic rim. The chemical and age profiles do not directly correspond, implying different diffusion rates between trace elements and U and Pb. The variation in core ages is interpreted to reflect radiogenic-Pb loss from a metamorphic population during new rim growth. The younger, c. 1800 Ma U-Pb age is interpreted to date new apatite growth from a compositionally distinct reservoir driven by tectonothermal and fluid activity, consistent with regional mica Ar-Ar ages. Results from these two samples show that recrystallization, dissolution and regrowth processes likely formed the younger rim overgrowths, and at temperatures below those often considered to be closure temperatures for Pb diffusion in apatite. The results from these samples imply many apatite grains may not record simple thermally activated Pb diffusion profiles and cautions against inversion of apatite U-Pb data to thermal histories without detailed knowledge of the grain growth/alteration processes.

1. Introduction

Apatite, a calcium phosphate mineral with the general formula $Ca_5(PO_4)_3(F,Cl,OH)$, is prevalent in both magmatic and sedimentary rocks and can be generated and modified during metamorphic processes. This crustal ubiquity, along with its ability to host U, means that apatite has become useful in a range of geochronology and thermochronology applications (Chew and Spikings, 2015; Corfu and Stone, 1998; Kirkland et al., 2017; Mark et al., 2016; Schoene and Bowring, 2007; Weisberg et al., 2018). Thermochronology can be considered to date when a mineral passes through a specific closure temperature for the isotope of interest (Dodson, 1973) and is a consequence of the integrated passage of a mineral through a daughter isotopes partial retention zone. In contrast, geochronology refers to the date at which a specific growth or alteration process may have affected a mineral. Unlike zircon, apatite can be readily found in silica-undersaturated mafic lithologies, however its U content is frequently much lower than that of zircon and apatite usually contains moderate to significant amounts of non-radiogenic (common) Pb. The high ratio of common to radiogenic Pb presents challenges for apatite U-Pb geochronology and calculated dates rarely have the precision of those obtained fromzircon (Chew et al., 2011; Glorie et al., 2017; Krogstad and Walker, 1994; LaFlamme et al., 2017). Nonetheless, apatite is still a very useful U-Pb chronometer as its typical closure temperature of around 375–600 °C (Cochrane et al., 2014; Schoene and Bowring, 2007) potentially

* Corresponding author.
E-mail address: c.kirkland@curtin.edu.au (C.L. Kirkland).

https://doi.org/10.1016/j.lithos.2018.08.007

can provide additional time-temperature constraints on retrograde or low-temperature prograde processes. Apatite can accommodate high concentrations of REE(Henrichs et al., 2018), Sr,Mn, Na, U, and Th, and other trace elements, making it potentially powerful in charting the trace element chemistry of the rock system (Fleet and Pan, 1997; Gawęda et al., 2014; Mao et al., 2016; Piccoli and Candela, 2002). So, as apatite is highly susceptible to a range of fluid-induced (metasomatic) changes that occur at variable pressures and temperatures (Harlov, 2015; Krenn and Finger, 2004; Nutman, 2007; Spear and Pyle, 2002), its chemistry linked to age may be powerful intracking fluid-rock interaction from the deep crust to near surface (Glorie et al., 2017; Henrichs et al., 2018; Kirkland et al., 2017; Schoene and Bowring, 2007). Metasomatic processes can be considered to affect the U-Pb system in apatite in two broad ways. Metasomatism may causenew growth of apatite, in which case the U-Pb geochronometer will record from the point that Pb stops diffusing out of the grain. Alternatively, metasomatism may cause partial to complete loss of radiogenic-Pb (potentially along with other chemical changes), in which case the U-Pb geochronometer will record either a mixed age or, if Pb loss is complete, the time of metasomatism.

2. Regional background

The Maniitsoq region, in southern West Greenland, lies immediately north of Nuuk and is a component of the North Atlantic craton, comprising the Mesoarchean Akia terrane (Fig. 1). The region is exceptionally well exposed, and in contrast to most other Archean cratons, which are dominated by low-gradegranite–greenstone associations, it is mainly tonalitic–trondhjemitic–granodioritic (TTG) orthogneiss and tholeiitic amphibolite, metasedimentary rocks, and ultramafic rocks, metamorphosed at amphibolite to granulite facies. The wider Nuuk region – including the Akia terrane – has been considered a classic example of Archean lateral tectonics and terrane accretion, whereby individual Archean tectono-stratigraphic terranes of different ages were assembled during the Neoarchean (Friend et al., 1996; Friend

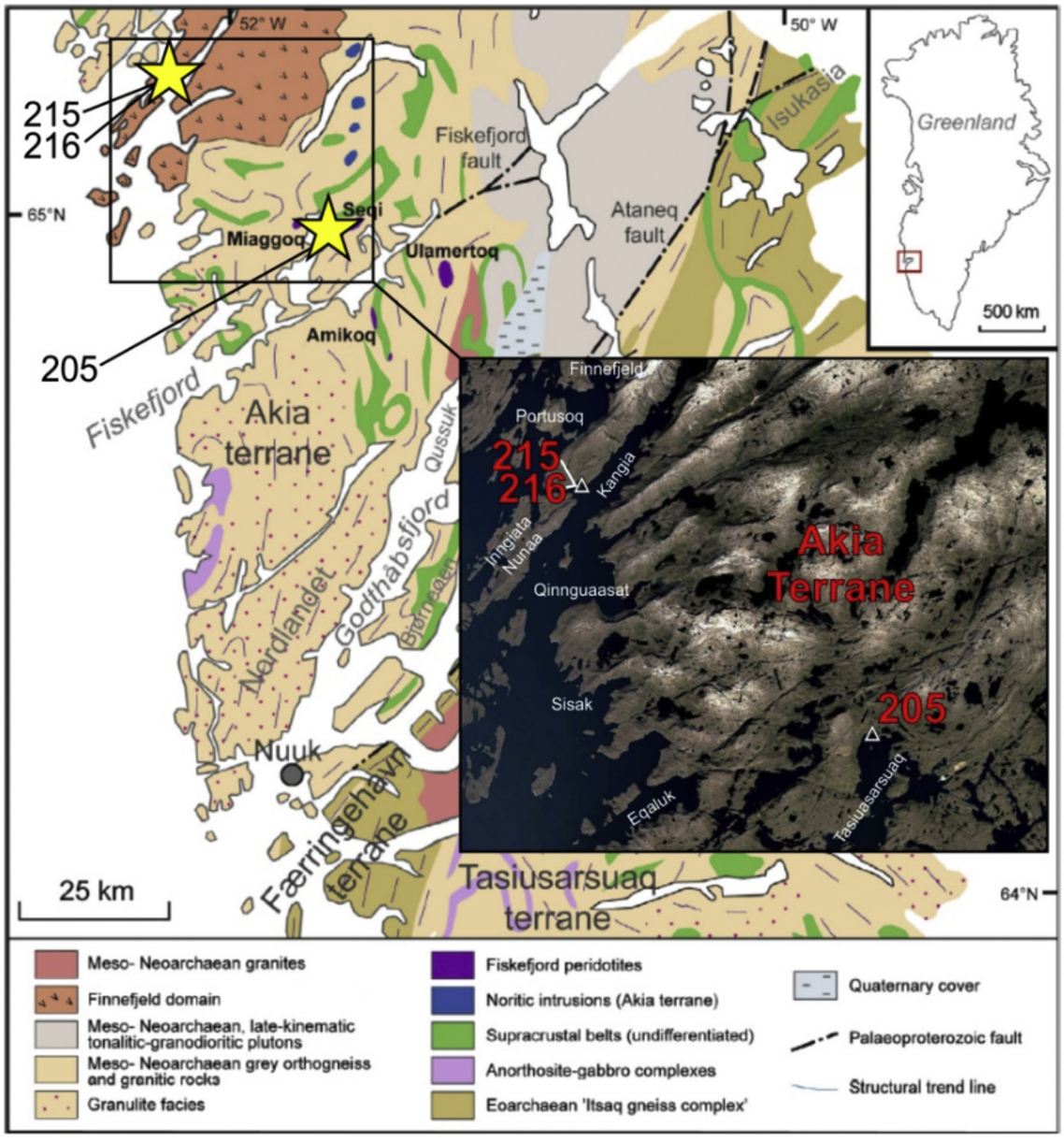

Fig. 1. Schematic geological map of southern West Greenland (from Szilas et al., 2015) showing the location of samples (yellow filled triangles). Inset shows Landsat image.

and Nutman, 2005). It has been proposed that the orthogneiss precursors of the North Atlantic craton were produced by slab melting of subducted oceanic crust (e.g. Garde, 1997; Winther and Newton, 1991, and references therein). Specifically, Garde et al. (2000) proposed that the AkiaTerrane developed by formation of a c. 3100 Ma magmatic arc over a Paleo- to Mesoarchean crustal core, followed by voluminous emplacement of Mesoarchean TTG gneisses and synchronous low-pressure granulite facies metamorphism and late-tectonic felsic magmatism. However, other models involving extra-terrestrial components have also been proposed for the Akia Terrane (Garde et al., 2014; Keulen et al., 2014; Scherstén and Garde, 2013) whereby a giant bolide impact at c. 3000 Ma was responsible for a prolonged Mesoarchean thermal reworking, and resulted in a range of melting and deformation features across the region. The Akia Terrane has also been regarded as the crustal link between Archean mid-crust, high-gradeorthogneiss–amphibolite associations exposed in West Greenland, and the lower-gradegranite–greenstone associations of the Superior Province of eastern Canada (Bridgewater and Schiøtte, 1991; Wilton, 1994).

The Akia Terrane comprises three distinct crustal components: a c.3200 Ma dioritic association, a c. 3.0 Ga TTG component (Garde et al., 2000), and a less than c. 2.9 Ga metasedimentary component (Kirkland et al., 2018). The majority of the orthogneisses are tonalite that was the basement for some, or tectonically intercalated with other, supracrustal rocks and associated mafic intrusive complexes. The supracrustal rocks consist largely of heterogeneous, compositionally layered rusty weathering metavolcanic amphibolite, metapelite to metapsammite, and metagabbroic and ultramafic rocks that represent disrupted layered intrusive complexes and overlying siliciclastic components. The supracrustal rocks were originally interpreted as remnants of oceanic crust, into which the precursors of the orthogneisses were intruded, presumably in a convergent plate-tectonic setting (Garde, 1990, 1997; Garde et al., 2000). However, recently many of the supracrustal rocks have been established as components of a package that is now known to be younger than the c. 3.0 Ga TTG association (Kirkland et al., 2018). In this work we use apatite from TTG and leucosome cutting the TTG to help address some of the complex history of overprinting metamorphism and fluid–rock interaction that has affected this region.

3. U-Pb geochronology

All U-Pb geochronology and geochemistry results are presented in Electronic Appendix Table 1.

3.1. Geochronology analytical method

3.1.1. Apatite

3.1.1.1. Spot analysis. Laser Ablation Inductively Coupled Plasma Mass Spectrometry (LA-ICP-MS) data collection for apatite age and trace elements, as single spot ablations, was performed during two sessions at the GeoHistory Facility in the John de Laeter Centre, Curtin University, Perth, Australia. Apatite was separated from samples using standard crushing and heavy liquid techniques. Individual apatite grains (mounted and polished in 1″ epoxy rounds) were ablated using a Resonetics RESOlution M-50A-LR, incorporating a Compex 193 nm excimer laser. The sample cell was flushed with ultrahigh purity He (350 mL min-1) and N_2(3.8 mL min-1), both of which were passed through an inline Hg trap. Isotopic intensities were measured using an Agilent 7700 s quadrupole ICP-MS, with high purity Ar as the plasma gas (flow rate 1 L min-1).

Apatite U-Pb age determination was performed first, with spot ablations in constant energy mode using a 50 μm spot and a 4 Hz laser repetition rate. Laser energy (measured at the sample surface) was 2 J cm^{-2}. After two cleaning pulses, each analysis comprised a 30 s background acquisition and 35 s of ablation. A total of 10 isotopes were determined (^{43}Ca, ^{44}Ca, ^{201}Hg, ^{202}Hg, ^{204}Pb, ^{206}Pb, ^{207}Pb, ^{208}Pb, ^{232}Th and ^{238}U). The dwell time on the Pb isotopes was 0.1 s with Ca isotopes measured for 0.03 s and Hg, U and Th measured for 0.0125 s. Laser induced U-Pb fractionation was accounted for during data reduction (Chew et al., 2014; Paton et al., 2010; Paton et al., 2011). McClure Mountain syenite apatite (Thomson et al., 2012) was used as the primary standard as it has moderate but reasonably consistent U and Th contents (~23 ppm and 71 ppm; (Chew and Donelick, 2012)), its thermal history is well known (it is the rock from which the ^{40}Ar/^{39}Ar hornblende standard MMhb is derived) and the crystallization age (weighted mean ^{207}Pb/^{235}U date of 523.51 ± 2.09 Ma) and initial Pb isotopic composition (^{206}Pb/^{204}Pb = 17.54 ± 0.24; ^{207}Pb/^{204}Pb = 15.47 ± 0.04) are known from high precision TIMS analyses (Schoene and Bowring, 2006). MAD Apatite (486.58 ± 0.85 Ma and 474.25 ± 0.41, (Thomson et al., 2012) and Duluth Complex apatite (U-Pb zircon age of 1099.1 ± 0.2 Ma, (Schmitz et al., 2003)) were used as secondary references, and analysed as unknowns. Ages obtained, by free regressions, on the secondary references Duluth Complex apatite (1112 ± 35; MSWD = 0.43; n = 24) and MAD apatite (489 ± 20; MSWD =0.45; n = 24) were within analytical uncertainty of recommended values.

Trace element ablations were placed over the previous U-Pb spot. Acleaning pulse was followed by 30 s of baseline acquisition and 45 s ablations, at a 4 Hz repetition rate using a 60 μm beam and laser energy of 2 J cm-2. Twenty-four isotopes were measured (^{29}Si, ^{31}P, ^{43}Ca, ^{44}Ca, ^{55}Mn, ^{88}Sr, ^{89}Y, ^{90}Zr, ^{139}La, ^{140}Ce, ^{141}Pr, ^{146}Nd, ^{147}Sm, ^{151}Eu, ^{157}Gd, ^{159}T, ^{163}Dy, ^{165}Ho, ^{166}Er, ^{169}Tm, ^{172}Yb, ^{175}Lu, ^{232}Th and ^{238}U), with most monitored for 0.02 s. Dwell time on Si and P was 0.01 s. International glass standard NIST 610 was used as the primary reference material for calculation of concentrations and to correct for instrument drift. ^{43}Ca was the internal standard element, assuming 39.36% Ca in apatite. Standard blocks were typically run after 20 unknown analyses. During the time-resolved analysis, contamination resulting from inclusions and compositional zoning were monitored and only the relevant part of the signal was integrated. Secondary trace element standard NIST 612, treated as an unknown, reproduced recommended values to within 2% for all elements except P (5%). The time-resolved mass spectra were reduced using Iolite (Paton et al., 2011, and references therein). All analyses were sited on the centre of apatite grains where a single ablation pit could be located without touching the enclosing epoxy resin.

As a means to assist in grouping analyses into growth or alteration populations, we calculate grain level ^{207}Pb corrected U/Pb dates and F207% values. We apply an iterative process to determine an appropriate common ^{207}Pb/^{206}Pb ratio to use in ^{207}Pb correction using the ^{207}Pb/^{206}Pb age only as an initial estimate for a model common Pb composition (Stacey and Kramers, 1975). We then use the initial estimated ^{207}Pb corrected age to revise the common Pb model value to calculate a new ^{207}Pb corrected ^{206}Pb/^{238}U age. We repeat this process until ages converge (Thomson et al., 2012). ^{207}Pb corrected ages on an individual spot level are treated as apparent ages only and we prefer to use a more conservative regression approach through the entire population to calculate dates onto which geological interpretation is placed. F207% values are calculated as the difference between the ^{206}Pb/^{238}U ratio for the ^{207}Pb corrected age and the measured ^{206}Pb/^{238}U ratio. Effectively this is the distance along a mixing line from radiogenic to common Pb where higher % represents a greater common component (Kirkland et al., 2017).

3.1.1.2. Depth profile. Apatite age and trace element depth profiles were also measured simultaneously from a single ablation volume using laser ablation split stream ICP-MS in a third session. The two selected apatite grains (mounted and polished in 1″ epoxy rounds) were ablated from the polished c-axis perpendicular apatite surfaces through to the underlying epoxy using the same Resonetics RESOlution M-50A-LR laser system but coupled to a Nu Plasma IImulti-collector inductively coupled plasma mass spectrometer (MC-ICPMS) for age determination and

also an Agilent 7700 quadrupole inductively coupled plasma mass spectrometer (Q-ICP-MS) for simultaneous trace element measurement. Laser system parameters are given in Table1. The sample cellwas flushed with ultrahigh purity He (350 mL min^{-1}) and N_2(3.8 mL min^{-1}), both of which were passed through an inline gold-based Hg trap. High purity Ar was used as the carrier gas (flow rate 1 L min^{-1}) and the ablated volume was split equally between the two mass spectrometers.

For age determination, the following elements were monitored (detector in brackets: H– Faraday Cup; IC– Ion Counter) over an 0.8 s integration time: ^{238}U (H10), ^{232}Th (H8), ^{208}Pb (IC0), ^{207}Pb (IC1), ^{206}Pb (IC2), ^{204}Pb (IC3), and ^{202}Hg (IC4). Each unknown apatite was bracketed by ablation of three standard blocks including the McClure Mountain syenite standard apatite (Thomson et al., 2012) and NIST 612 glass both of which were used as primary reference materials. Durango (31.44 ± 0.18 Ma, (McDowell et al., 2005) was included as a secondary standard. The time-resolved mass spectra were subdivided into eight equal time segments of 20 s each (approximate ablation depth of 20 μm for each slice). The McClure Mountain syenite and NIST612 standards were treated similarly. Each segment in the unknowns was processed against the same time segment in the standard grains (e.g., first 20 s segment in the apatite unknown was processed against first 20 s segment for the standards) so that downhole fractionation corrections were always started at the same ablation depth/time in the standard and sample material. In addition, fractionation of $^{207}Pb/^{206}Pb$ and $^{238}U/^{206}Pb$ was also monitored and corrected with reference to NIST 612, the advantage here over natural apatite being that the glass has a fixed common to radiogenic Pb ratio. Ages were derived for each time segment using Iolite 3.5 (Paton et al., 2011) with the VizualAge_UcomPbine DRS(Chew et al., 2014) and in-house Microsoft Excel macros with ^{207}Pb corrections calculated as described above except common Pb was defined from the upper intercept of the spot analysis in the same sample (discussed in detail below). Excluding one aberrant step (step 3; 34 ± 1 Ma) 207 corrected ages for the Durango secondary reference reproduced the accepted age within analytical uncertainty (31.6 ± 0.7 Ma; MSWD 2.4). Full instrument setup is given in Table1.

For trace element determination a total of 24 isotopes were measured (^{29}Si, ^{31}P, ^{43}Ca, ^{44}Ca, ^{55}Mn, ^{88}Sr, ^{89}Y, ^{90}Zr, ^{139}La, ^{140}Ce, ^{141}Pr, ^{146}Nd, ^{147}Sm, ^{151}Eu, ^{157}Gd, ^{159}T, ^{163}Dy, ^{165}Ho, ^{166}Er, ^{169}Tm, ^{172}Yb, ^{175}Lu, ^{232}Th and ^{238}U), with most monitored for 0.02 s. Dwell time on Si and P was 0.01 s. International glass standard NIST 612 was used as the primary reference material for calculation of concentrations and to correct for instrument drift with ^{43}Ca utilized as the internal standard element, assuming 39.36% Ca in apatite. NIST 614 was also analysed as a secondary standard. Standard blocks bracketed the two apatite unknowns and were treated similarly to samples. As with the age determination, 8 equally spaced time segments were selected over the full length of the ablation period, matching the segments selected for age determination. Each segment in the unknowns was processed against the corresponding time segment in the standard glass. The time-resolved mass spectra were reduced using the Trace Elements data reduction scheme in Iolite 3.5 (Paton et al., 2011 and references therein). Isotopic concentrations for the NIST 614 secondary standard (^{29}Si internal reference isotope) were reproduced to within 7% of the accepted value for most isotopes with considerably better precision on some (e.g., Sr - 1.4%, U– 3.4%).

Table 1
Instrument parameters for apatite laser ablation split stream ICPMS

Nu Plasma II MC ICPMS	Nu Instruments Ltd., Wrexham, UK
RF forward power	1300 W
RF reflected power	3 W
Coolant	13 L/min
Carrier gas (Ar)	0.9 L/min
Make up gas (He+N_2) flow	320 mL min^{-1} (He); 1.2 mL min^{-1} (N_2)
Monitored masses	^{238}U (H10), ^{232}Th (H8), ^{208}Pb (IC0), ^{207}Pb (IC1), ^{206}Pb (IC2, ^{204}Pb (IC3), ^{202}Hg (IC4).
Dwell Time	115 ms
Integration	0.8 s
Agilent 7700× quadrupole ICPMS	Agilent Technologies
Sample Introduction	Ablation aerosol
RF power	1500 W
Make up gas (He+N_2) flow	0.7 L/min Ar
Detection system	EM detector
Monitored masses	^{29}Si, ^{31}P, ^{43}Ca, ^{44}Ca, ^{55}Mn, ^{88}Sr, ^{89}Y, ^{90}Zr, ^{139}La, ^{140}Ce, ^{141}Pr, ^{146}Nd, ^{147}Sm, ^{151}Eu, ^{157}Gd, ^{159}T, ^{163}Dy, ^{165}Ho, ^{166}Er, ^{169}Tm, ^{172}Yb, ^{175}Lu, ^{232}Th,^{238}U
Integration time per peak	200 ms (except Si, P and Ca = 100 ms; Mn and Sr = 400 ms)
Total integration time per reading	0.5 s
RESOlution 193 nm Excimer Laser	ASI Ltd., Canberra, Australia
Laser	Compex 102 excimer
Cell	Lauren Technic S155
Fluence	1.8 J/cm^2
Repetition rate	4 Hz
Excavation rate	~0.8 μm/pulse
Delay between analyses	45 s
Ablation duration	40 s

3.1.2. Zircon

3.1.2.1. Spot analysis. LA-ICPMSU-Pb analysis of sample 215 zircon grains was also performed at the GeoHistory Facility in the John de Laeter Centre. Individual zircon grains were ablated using the same Resonetics RESOlution M-50A-LR sampling system as was utilized for apatite ablation. Samples were ablated for 30 s at a 7 Hz repetition rate using a 50 μm beam spot and laser energy of 1.5 J/cm^2. A20 s period of background analysis was acquired prior to ablation. The sample cell was flushed by ultrahigh purity He (350 mL min^{-1}) and N_2(3.8 mL min^{-1}). Isotopic intensities were measured using an Agilent 7700 s quadrupole ICPMS, with high-purity Ar as the plasma gas (flow rate 0.98 L min^{-1}). The dwell time for all masses was 0.01 s. The primary reference material used for zircon U-Pb dating in this study was the OG-1 zircon standard (3465.4 ± 0.6 Ma; (Stern et al., 2009)) with the following secondary zircon standards: Plešovice (337.13 ± 0.37 Ma; Sláma et al., 2008), R33 (419.26 ± 0.39 Ma; Black et al., 2004), and GJ-1(601.7 ± 1.4 Ma; Jackson et al., 2004). $^{206}Pb/^{238}U$ ages calculated for all zircon age standards, treated as unknowns, were within 3% of the accepted values. For example, the mean $^{206}Pb/^{238}U$ age determined for Plešovice was 327 ± 10 Ma (2σ, n = 12, MSWD = 1.0), within uncertainty of the recommended value. The time-resolved mass spectra were reduced using the U/Pb Geochronology3 data reduction scheme in Iolite (Paton et al., 2011). No common lead corrections were deemed necessary due to low ^{204}Pb counts.

SIMS U-Pb analysis of sample 216 zircon grains were performed on Shrimp B in the John de Laeter Centre following analytical protocols matching those discussed in Wingate and Kirkland (2015). Eight analyses of the BR266 standard (Stern, 2001) were obtained during the session, which indicated an external spot-to-spot (reproducibility) uncertainty of 0.56% (1σ), and a $^{238}U/^{206}Pb^*$ calibration uncertainty of 0.31% (1σ). Calibration uncertainties are included in the errors of $^{238}U/^{206}Pb^*$ ratios and dates listed in Appendix Table1. Two analyses of the OG-1 standard yielded a $^{207}Pb/^{206}Pb$ weighted mean age of 3464 ± 3 Ma (MSWD = 0.96) identical to the accepted value. Common-Pb corrections were applied to all SIMS analyses using contemporaneous isotopic compositions determined according to the Pb evolution model of Stacey and Kramers (1975).

3.2. Geochronology results

3.2.1. Single grain U-Pb and geochemistry

3.2.1.1. 205 tonalitic gneiss (apatite). Sample 205 is from a homogeneous tonalitic gneiss that cuts older foliated metadioritic gneiss. The sample was recovered from coastal outcrop 96 km due north of Nuuk and 32 km north-east of Atammik (Fig. 1). Apatite in this sample displays homogeneous textures under BSE, but distinct zonation in CL (Fig. 2). Based on mineral liberation analysis with a Telscan TIMA, apatite grains are up to 208 μm (c-axis parallel), with a mode of <5 μm, although 31% are >40 μm. The modal abundances of minerals, as observed in thin section, are 48% plagioclase (An_{81}), 24% quartz, 20% alkali feldspar (Or_{89}), 7% mica (biotite and muscovite equally present), and 1% accessory minerals such as epidote, apatite, and titanite. Epidote is developed both at grain boundaries, but mostly as discrete grains. Quartz is granoblastic with undulose extinction. Feldspars are generally fresh, although with minor clay minerals within fractures and epidote along grain boundaries when in contact with mica (Fig. 3).

U-Pb analyses of apatite define a broad discordia array that scatters significantly with F207% ranging from 5 up to 56%, interpreted as principally reflecting mixing between radiogenic and common Pb. Not only do the data scatter between radiogenic and non-radiogeniccomponents but also, towards the radiogenic end of the mixing array (i.e. lower $^{207}Pb/^{206}Pb$) display increased U/Pb variability at a given Pb/Pb ratio (Fig. 4). This variability in U/Pb ratios is mirrored in the apatite Mn content, which defines a continuum of concentrations from 176 to 385 ppm Mn. A high Mn group (>335 ppm) yields a lower intercept on concordia of c. 2813 Ma (MSWD = 0.44) and an upper intercept $^{207}Pb/^{206}Pb_c$ ratio of 1.115 ± 0.12. A low Mn group (with an arbitrary <250 ppm Mn cut off) illustrates a younger age with lower intercept of c. 2149 Ma (MSWD = 1.5) and an upper intercept $^{207}Pb/^{206}Pb_c$ ratio of 1.056 ± 0.09 (Fig. 4). Both upper intercepts are similar in terms of common Pb composition but the radiogenic Pb component is distinctly different with apparent ages that vary by at least >400 Ma. Those analyses with low Mn and younger apparent ages indicate lower La_N/Sm_N ratios, indicative of more steeply negative LREE profiles. Apatite from sample 205 is, in general, characterized by positive Eu anomalies.

3.2.1.2. 216 granitic leucosome in gneiss (zircon and apatite). Sample 216 is from a folded granitic leucosome that intrudes dioritic to tonalitic gneisses. The sample was recovered from a coastal outcrop 2.6 km south-east of Ikerasak and 44 km north-east of Atammik. In thin section, this sample contains about 38 vol% quartz, 30% alkali feldspar (Or_{73}), 22% plagioclase (An_{24}), 9% biotite, and accessory epidote and opaque oxide minerals. A distinct foliation is defined by alignment of biotite. Epidote is rare and only found as isolated grains at the interface between plagioclase and biotite. Feldspars are generally fresh with minimal retrogression.

Zircon crystals in this leucosome are subhedral to euhedral and, in CL images, idiomorphic zoning is ubiquitous and most grains have low CL response (high U)overgrowths up to 30 μm thick. Four analyses (Group M)of homogenous rims yield a weighted mean $^{207}Pb/^{206}Pb$ age of 2994 ± 5 Ma (MSWD = 1.3), interpreted as the age of leucosome crystallization. The uranium content of Group M rims is on average c.900 ppm, some c. 700 ppm greater than the cores. Ten analyses (Group X)of idiomorphically zoned zircon yield a weighted mean $^{207}Pb/^{206}Pb$ age of 3059 ± 6 Ma (MSWD = 2.4), interpreted as the magmatic crystallization age of an inherited component incorporated into this leucosome. Two analyses (Group P)yield $^{207}Pb/^{206}Pb$ ages of2981 ± 4 Ma and 2718 ± 18 Ma (1σ) and are interpreted to reflect ancient radiogenic-Pb loss (Fig. 5; Appendix Table1).

Apatite in this sample is euhedral and displays homogeneous textures in BSE images and can be up to 268 μm in size, with a mode of c. 50 μm. Apatite is also homogeneous in CL images (Fig. 2). U-Pb analyses of apatite broadly define two discordia arrays that scatter between radiogenic and non-radiogenic components. An apparently older array scatters between 3 and 13% F207. This apparently older component (19 analyses) has Sr concentrations of >224.4 ppm and defines a regression that yields a lower intercept on concordia of c. 2493 Ma and an upper intercept $^{207}Pb/^{206}Pb_c$ ratio of 0.93 ± 0.27 (MSWD = 0.51). Adistinct younger discordia array (41 analyses) has lower Sr content of

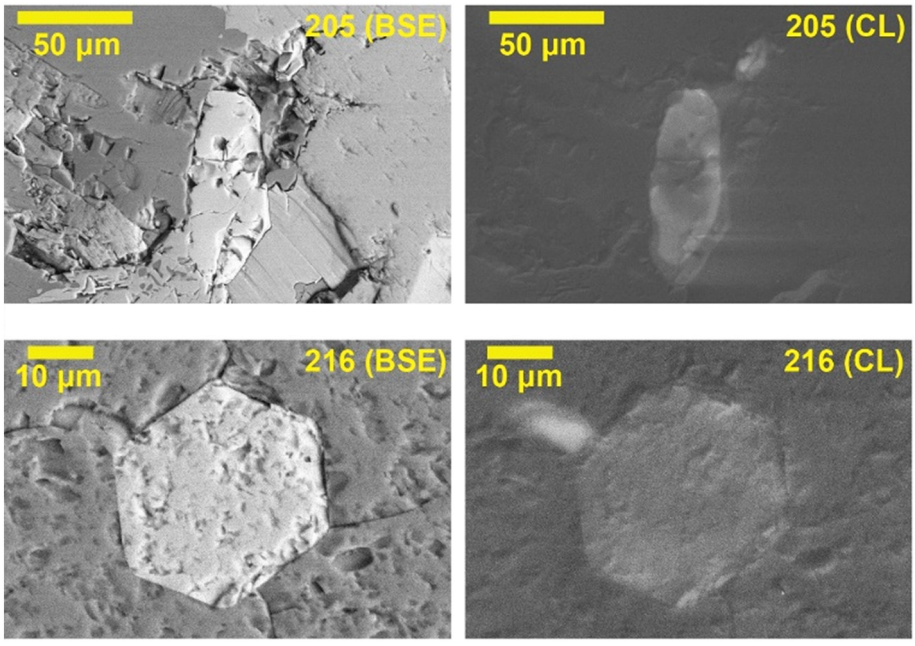

Fig. 2. Left; backscatter electron images of apatite from the Akia Terrane. Right; cathodoluminescence images of the same apatite. Note presence of clear overgrowths and embayed margin on sample 205 apatite. BSE: Backscatter-electron image, CL: Cathodoluminescene image.

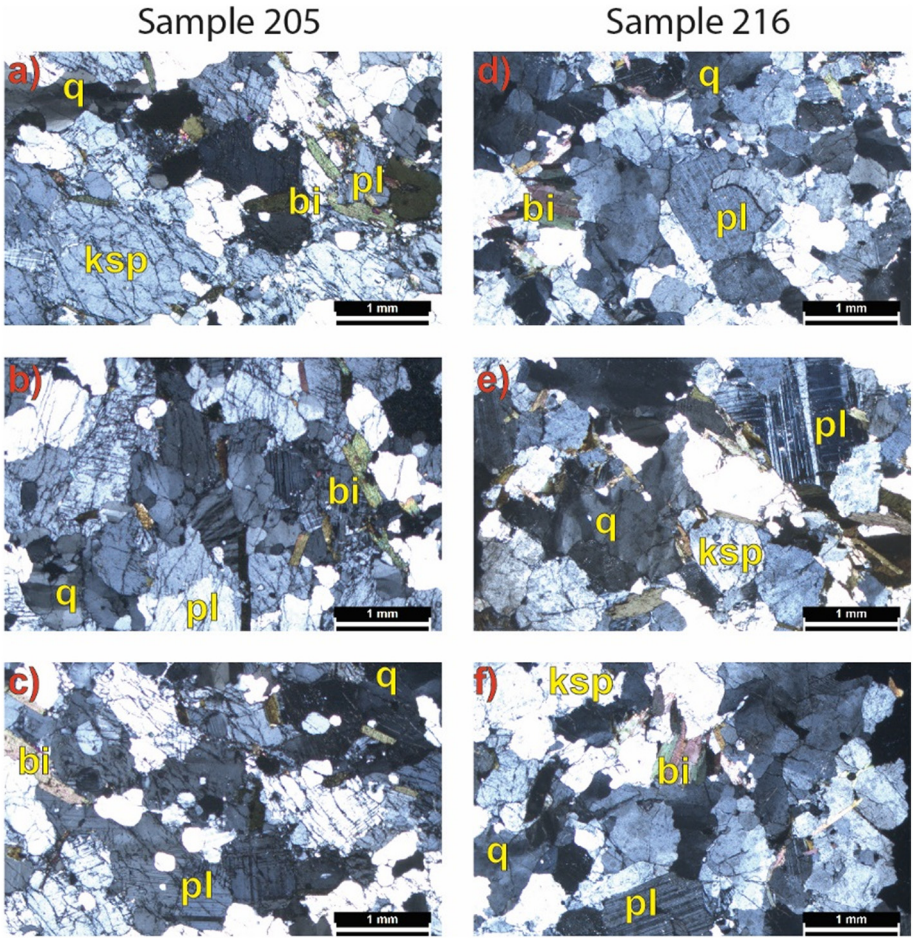

Fig. 3. Left; Series of photomicrographs of sample 205, tonalitic gneiss. The modal abundances as observed in thin section are 48% plagioclase (An_{81}), 24% quartz, 20% alkali feldspar (Or_{89}), 7% mica (biotite and muscovite equally present), and 1% accessory minerals such as epidote, apatite, and titanite. Right; sample 216, granitic leucosome in dioritic to tonalitic gneisses. Inthin section the modal abundances are about 38% quartz, 30% alkali feldspar, 22% plagioclase, 9% mica (all biotite), and accessory epidote and opaque oxides. Mineral abbreviations: bi = biotite, q = quartz, pl = plagioclase, ksp = K-feldspar.

<211.1 ppm and yields a lower intercept of c. 1805 Ma (MSWD = 0.37) and an upper intercept $^{207}Pb/^{206}Pb_c$ ratio of 1.165 ± 0.13. Analyses in this group range from 6 to 37% F207 (Fig. 4). 19 analyses lie between these two groupings with both intermediate apparent age and Sr contents. The upper intercept for the older array is imprecisely defined and may not be identical in terms of common Pb composition to the younger array. Furthermore, the radiogenic Pb component is distinctly different between the two arrays with apparent ages that vary by over 500 Ma. Those analyses with low Sr and younger apparent ages correlate with lower total REE content. Furthermore, older apparent ages are associated with higher U content on average, consistent with the lower analytical uncertainties on U/Pb isotopic ratios for these analyses.

3.2.1.3. 215 late granite sheet (zircon). Sample 215 is from a structurally late granite sheet that intrudes leucosome- bearing dioritic to tonalitic gneisses. This sample was taken from a few meters away from sample 216. The sheet cuts both the foliation and leucosomes in the host gneiss. The zircon crystals are euhedral with length to width ratios up to 6:1. In CL images the grains show moderate CL response with oscillatory zoning particularly evident in partially resorbed cores. Most grains have a low CL outermost zone. Four analyses are >10% discordant (Group D). These analyses are not considered further. Twenty-two analyses (Group I)yield a weighted mean $^{207}Pb/^{206}Pb$ age of 2558 ± 8 Ma (MSWD = 1.8), interpreted as the age of granite crystallization. Nine core or discrete grain analyses (Group X)yield $^{207}Pb/^{206}Pb$ ages of 3050–2628 Ma, interpreted to reflect inherited zircon (Fig. 5). Five analyses (Group P)yield $^{207}Pb/^{206}Pb$ ages of 2489–2319 Ma and indicate extreme U and Th content. Many of these analyses are on fractures. These analyses are interpreted to have experienced ancient radiogenic-Pb loss.

3.2.2. Apatite depth profiles

In order to better understand the apatite U-Pb geochronology two grains were chosen for depth profiling. The depth profile analyses penetrated through the grain from the polished surface (half grain thickness) into the epoxy and were standardised over the depth interval in which a corresponding reference was ablated. ^{207}Pb corrected ages have been calculated for a sequence of integration steps for both samples. These apparent ages are based on a regression anchored through the upper intercept of the quadrupole single spot ablation regressions, which indicate a common $^{207}Pb/^{206}Pb$ ratio of 1.089 for sample 205 and 1.165 for sample 216, which is interpreted as the best estimate of the common Pb composition.

The apparent age profile of sample 205 rises to ages as old as c.2935 Ma before falling towards the rim with a youngest age of c.2277 Ma (Fig. 6). The La_N/Sm_N ratio for all integrations is >0.5. Concentrations of Mn are >460 ppm and rise towards the rim, which corresponds to the chemical signature in the older of the single spot grain analyses. U content is about 6 ppm until a rim that has >20 ppm. An integration (step 9; Appendix Table1) was selected to just characterize this rim and yields an apparent age of 2277 ± 37 Ma. The core region with uniform U content indicates relatively consistent apparent ages that yield a weighted mean age of 2705 Ma with slight excess dispersion (MSWD = 3). The consistency of these core ages and compositional

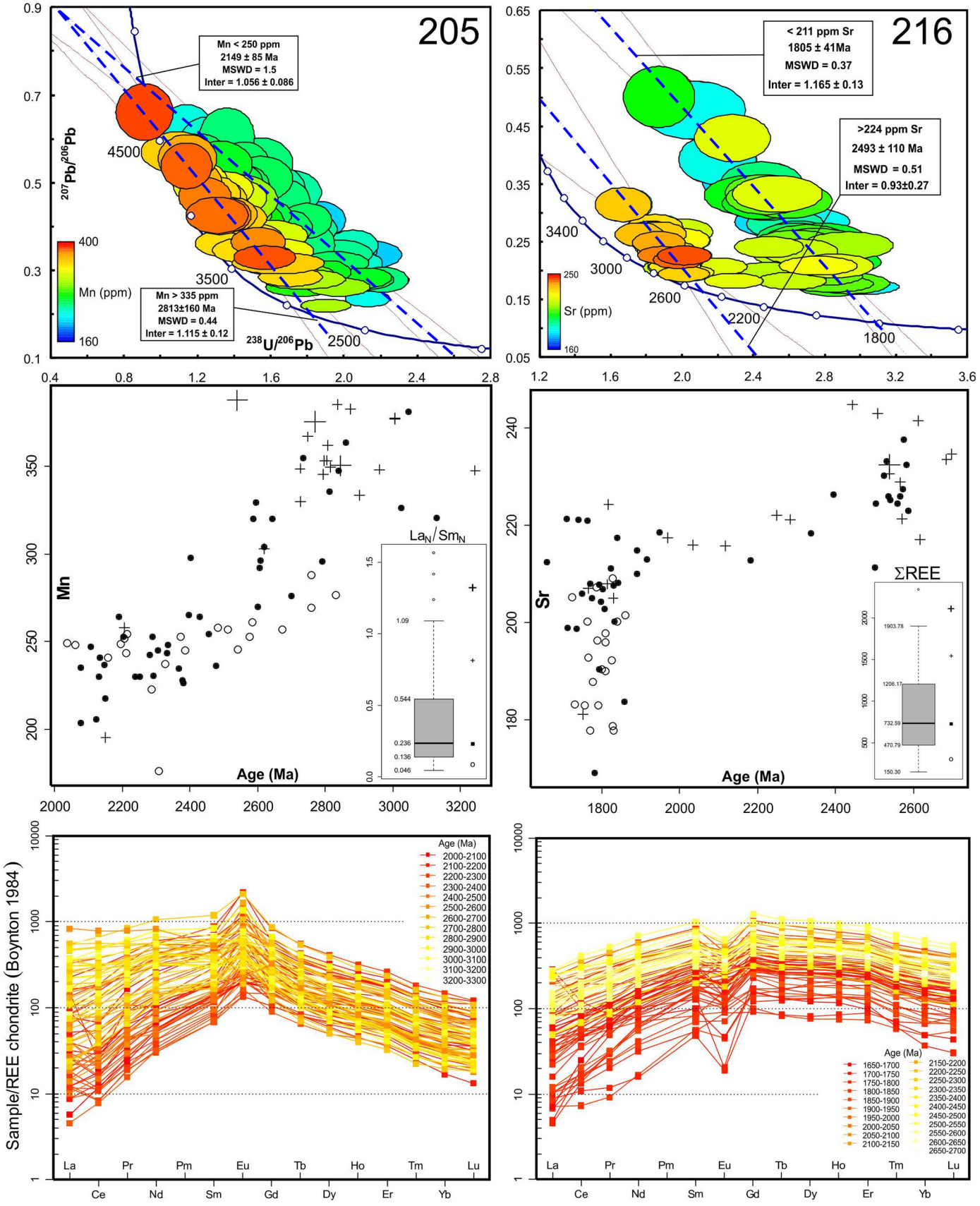

distinction from the rims is consistent with core cooling through the radiogenic Pb retention temperature for a magmatic crystal across atimescale which did not allow any obvious Pb diffusion profile to develop on the grain scale. The apparent age profile of sample 216 rises to an age of 2031 Ma before falling to ages around 1700 Ma with increasing ablation depth (e.g. towards the rim). Concentrations of Uand Th gradually decrease with ablation depth (towards rim) with the content of both spiking in the last two integrations, reflecting anenriched

rim. Sr broadly falls with integration step. La_N/Sm_N values fall until the last two integrations (Fig. 6). REE patterns are similar in all ablations but the total REE concentration is significantly higher in the last two integrations. The chemical profiles and apparent ages do not directly correspond (e.g. older zones are not necessarily geochemically distinct), consistent with different diffusion rates between trace elements and U and Pb. Nonetheless, based on Th, U,REE concentrations, two distinct zones are apparent: an inner zone corresponding approximately to the core of the grain and a rim enriched in Th, U and REE. The core region shows apparent ages which peak at c. 2000 Ma but decrease away from this high, consistent with radiogenic Pb loss. The rim yields apparent ages of c. 1735 Ma, similar to the apparent ages in the immediately adjacent core region. The broad trend in the core age profile could be considered broadly consistent with some form of disturbance event (thermal, recrystallization, or dissolution driven) causing radiogenic-Pb mobility synchronous with neoblastic apatite rim growth. The higher U content of the rims corresponds with greater radiogenic-Pb in the rims and a position on the concordia diagram that is closer to the radiogenic end of a mixing array. The oldest core apparent age provides a minimum age for original apatite crystallization at >2031 Ma.

4. Phase equilibria modelling

4.1. Pseudosection methods

Phase equilibria modelling is used to bracket the P–T conditions ofmetamorphism and fluid influx potentially responsible for apatite dissolution-regrowth in sample 205. Modelling was conducted in the NCKFMASHTO system—applicable for mafic to intermediate compositions (Palin et al., 2016)—using the internally consistent thermodynamic database (ds63) of (Holland and Powell, 2011) and the THERMOCALC (v.3.45) software package (Powell et al., 1998). Activity–composition models are from Green et al. (2016). Phases modelled as pure end-members are quartz, rutile, titanite and aqueous fluid (H_2O). All mineral abbreviations are from (Holland and Powell, 2011) except for titanite (ttn). Bulk rock compositions were determined at ALS Laboratories (Ireland) using their ME-ICP06 analytical package. Samples were digested by lithium metaborate fusion and major element concentrations were determined by ICP-AES. The amount of ferric iron was assumed to be 10% and water was set to be in excess. The measured and modelled compositions are summarized in Table2.

4.2. Pseudosection results

A P–T pseudosection for sample 205 and water-saturated conditions is shown in Fig. 7a. At 0.2 to 0.9 GPa, the mineral assemblage at the wet solidus (~650 °C) is predicted to be dominated by plagioclase, quartz and K-feldspar with ~5 mol% (approximately equivalent to vol%) biotite and < 1 mol% rutile and muscovite. These predicted mineral proportions are generally consistent with the observed modes in the sample. At $P >$ 0.9 GPa, the calculated solidus assemblage includes minor amounts of epidote and titanite. Below the solidus, a relatively low-variance field extends from 450 °C at 0.1 GPa up to the solidus at 0.9 GPa that represents the down-temperature breakdown of plagioclase to albite and epidote. Normalized molar proportions of the phase assemblages at 0.4 GPa (Fig. 7b) show the general reaction sequences and mineral proportions as a function of temperature. Plagioclase breakdown to albite is expected to occur from ~550–470 °C, and plagioclase breakdown to epidote and albite from ~520–470 °C. K-feldspar is predicted to break down to muscovite over a similar temperature range. The temperature ranges of these reaction fields increase with increasing pressure.

The presence of grain boundary epidote associated with plagioclase restricts any fluid infiltration in sample 205 to temperatures lower than the set of low-variance fields in Fig. 7a, i.e. to $T >$ 450 °C at 0.1 GPa and $T >$ 600 °C at 0.8 GPa. Regional Neoarchean peak metamorphic conditions are 820–850 °C at 0.8–1.0 GPa and represent an apparent thermal gradient of ~1000 °C/GPa (Kirkland et al., 2018). Extrapolation along this gradient from peak conditions results in pressures of ~0.65 GPa at the wet solidus (~650 °C) and at 0.55 GPa at the epidote-in phase boundary

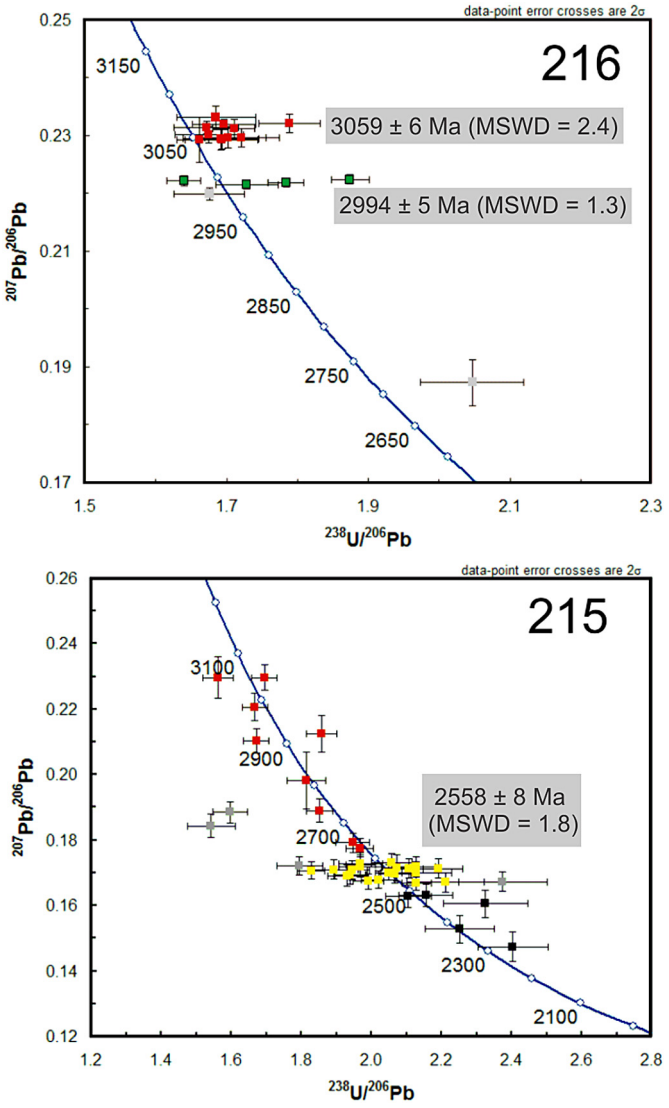

Fig. 5. U-Pb analytical data for zircons from samples 216: Leucosome, and 215: Granite sheet. Yellow squares indicate Group I (magmatic zircon); red squares indicate Group X (inheritance); green squares indicate Group M (zircon dating metamorphism); black squares indicate Group P (radiogenic-Pb loss); grey squares indicate Group D (discordance >10%).

Fig. 4. Upper; inverse U-Pb concordia diagrams for sample 205 (left) and 216 (right). Two sigma error ellipses are colour scaled for chemistry (Mn concentration 205; Sr concentration 216). Best fit linear regression through chemically defined groups is indicated by a blue dashed regression line, with red solid line indicating the two sigma uncertainty bound of the regression line. Middle; anomaly plot (left 205, right 216). Inset in anomaly plot is a box and whisker diagram for the defined chemical parameters with symbols scaled to median, quartiles and outliers. Symbols on anomaly plot defined as per inset box and whisker diagram. Lower: chondrite normalized REE plots (left 205, right 216). REE profiles are colour scaled according to ^{207}Pb corrected age. Note for 205 the average LREE slope increases with younger apparent ages and for 216 the total REE decreases with younger apparent ages.

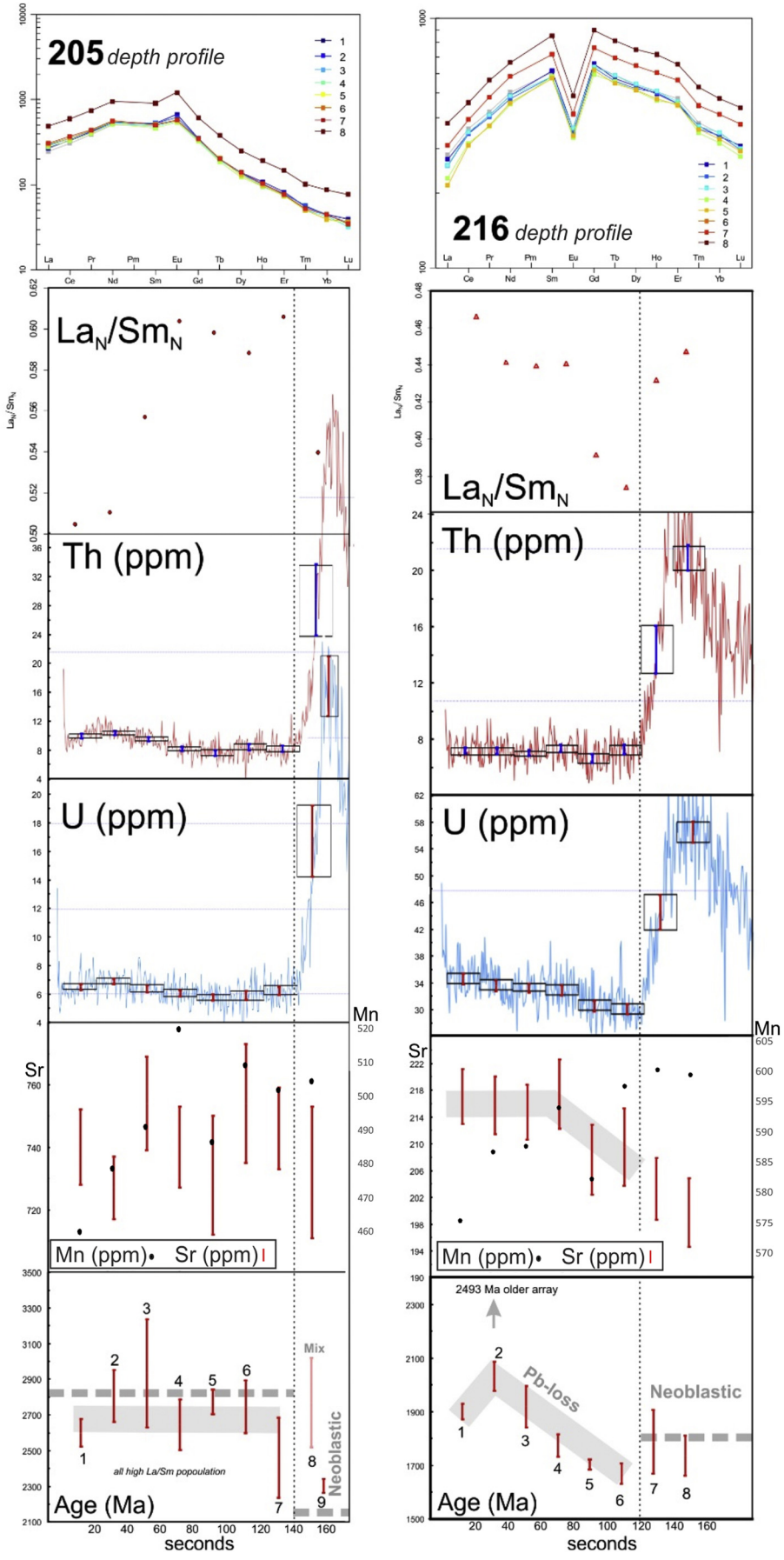
205 depth profile
216 depth profile
La Pr Pm Eu Tb Ho Tm Lu
Ce Nd Sm Gd Dy Er Yb
1 2 3 4 5 6 7 8
La_N/Sm_N
Th (ppm)
U (ppm)
Mn
Sr
Mn (ppm) Sr (ppm)
Age (Ma)
all high La/Sm popoulation
Mix
Neoblastic
2493 Ma older array
Pb-loss
seconds

(~550 °C). Considering the value of the apparent gradient is a maximum due to thermal relaxation after the peak of metamorphism, the minimum temperature of fluid infiltration into sample 205 to preserve the observed plagioclase- and epidote-bearing assemblage is ~550 °C. However, this does not apply if a separate thermal pulse was associated with fluid infiltration responsible for apatite recrystallization. In this scenario, the temperatures would still need to be >450 °C to preserve the observed mineral assemblage in the presence of a free hydrous fluid phase.

5. Discussion

5.1. Summary of U-Pb results

Sample 205, from a tonalitic gneiss, reveals distinct rims under CL(Fig. 2). U-Pb analyses define a broad discordia array interpreted to reflect mixing between radiogenic and common components (Fig. 4). The U-Pb data also reveals significant scatter at the radiogenic end of the array. This scatter in U-Pb space correlates with Mn chemistry, with a high Mn group yielding an old age of c. 2813 Ma whereas a lower Mn group yielding a younger age of c. 2149 Ma (Fig. 4). Importantly, both upper intercepts are similar in terms of common Pb composition. Depth profiling of this apatite reveals older apparent ages in the core before younger ages towards a U enriched rim with a best age estimate of c. 2277 Ma. The chemistry, morphology, depth profiling and spot analysis results imply these crystals were originally igneous and whose cores now record a cooling age, with discrete high U rims reflecting later new apatite growth (Fig. 8). The dominant c. 2800 Ma age of high Mn apatite in sample 205 might be considered as reflecting some sort of average time of cooling to the Pb diffusion temperature. However, these apatite grains do not solely record thermally activated volume diffusion of Pb as a dissolution-regrowth process is indicated by a younger rim overgrowth (Fig. 6). The small amount of epidote observed in the sample implies a < 600 °C fluid infiltration event associated with the apatite rims.

In contrast to sample 205, sample 216 from a granitic leucosome is homogeneous in CL images. However, U-Pb analyses define two discordia arrays with potentially distinct common Pb components (Fig. 4). An older array with age of c. 2490 Ma has elevated Sr concentrations whereas a younger c. 1800 Ma array has lower Sr content. Theyounger array is also associated with lower total REE content. The younger apatite array may have sourced older crustal Pb in comparison to the older apatite cores. A depth profile through an apatite grain from sample 216 rises to an apparent age of 2031 Ma before falling to late Paleoproterozoic ages towards the rim (Fig. 6). In the depth profiles, trace element compositions and apparent ages do not directly correspond (e.g. older zones are not necessarily geochemically distinct), although there is a broad similarity, consistent with somewhat different diffusion rates between trace elements and U and Pb (Fig. 6). Specifically, the diffusion closure temperatures of Sr and REEs in apatite aresignificantly higher than Pb (Cherniak, 2000). The core region isinterpreted to reflect radiogenic-Pb loss at the same time as new rim growth. The higher U content of the c. 1800 Ma rims corresponds with a greater portion of radiogenic-Pb. The common Pb content in the younger apatite array implies interaction with a distinct, more radiogenic, crustal source (Fig. 4). This observation cautions that using intra-grain mixing lines to define common Pb corrections must be cognisant of the potential for even individual grains to have different common Pb reservoirs dependant on the growth environment of that apatite domain.

5.2. Apatite Pb diffusion or dissolution and new growth

A range of different growth and alteration processes can be identified from the linked geochronology and chemistry signatures in these apatite crystals. It is pertinent to note that the spot analyses need not directly correspond to the age and chemistry of the depth profiles. For example there is generally lower La/Sm ratios in the younger end-member of the individual grain apatite analyses from sample 205, however in the depth profile there is little distinction between core and rim. The Mn concentration trend with age is also apparently opposite in thedepth profile versus individual spot analyses. The depth profile for sample 216 also shows some distinctions from the individual analyses, specifically the Sr depleted rim with young age has enriched total REE relative to the core, while a depletion in total REE concentration is recorded in the low Sr, young individual analyses (Fig. 6). Th and Uare also high in the rim of sample 216 (Fig. 6) while the individual analyses from sample 216 that are young tend to be lower in Th and U(Appendix Table1). Such observations imply that the thin high U rims in both samples were below the individual grain spot's spatial resolution. Nonetheless, there is relatively good age correspondence which may imply alteration processes recorded in cores were synchronous with new growth processes.

5.2.1. Thermally activated Pb diffusion

Two general conditions of thermally activated diffusion can be considered in response to decreasing temperature and a minerals passage through its partial retention zone: A)If the rate of homogenization of composition by diffusion within the mineral fails to keep up with the rate of change of the interface composition then the mineral would not have a single closure temperature, but a closure temperature profile (e.g. a slow cooling situation). B)Conversely, if the mineral passes rapidly through its partial retention zone then a single closure age may be recovered. The c. 2800 Ma age of apatite in sample 205 is interpreted as the time of cooling to the Pb diffusion temperature in some grains given the crystallization age of c. 3000 Ma for tonalitic gneisses in the Akia Terrane (Garde, 2007; Garde et al., 2000) and 820–850 °C, 8–10 kbar, regional metamorphism (Kirkland et al., 2018) which must have occoured prior to or at c. 2800 Ma in this sample. This interpretation of an original magmatic genesis for sample 205 apatite is consistent with its geochemistry; the Sr contents, REE patterns and Eu anomalies of magmatic apatite have been considered to directly relate to the geochemical composition of its parental magma, reflecting magma mixing and compositional heterogeneity in the magma source region. Magmatic apatite REE patterns commonly exhibit negative Eu anomalies, a function of the redox state of the magma and feldspar fractionation. A positive Eu anomaly is not related to fractionation processes but must be a source feature (Chu et al., 2009). Apatite in sample 205 has a distinctive positive Eu feature (Fig. 4) which is also seen in the whole rock composition of this tonalitic gneiss (Fig. 9), consistent with a magmatic source comprising feldspar cumulates. The value of ($Sr_{apatite}/Sr_{whole\text{-}rock}$) for apatite in sample 205 is <1 which is also consistent with its felsic source (Chu et al., 2009). The depth profile for sample 205 apatite is relatively flat implying a single cooling age for this grain yet the individual spots from multiple grains reveal significant age variation. We interpret these features to imply a short transit time through the partial retention zone (i.e. Condition B), yet different Pb closure temperatures between grains, likely a consequence of grain size (Blackburn et al., 2011).

In contrast to sample 205, apatite core depth profiles from sample 216 do appear to yield a Pb diffusion profile (see also Cochrane et al., 2014). Such profile implies Pb diffusion which could not be accommodated by transport over a finite timescale into the matrix (i.e. Condition

Fig. 6. Time resolved ablation signal for various chemical, isotopic and derived parameters measured in depth profiling. Left sample 205, right sample 216. Upper, REE plots colour coded for ablation integration step depth. Higher step value indicates a deeper ablation and a position closer to the grain margin. Lower, ablation depth profiles. Values are fractionation corrected at each respective integration interval. Integration intervals shown as black boxes on Th and U signals, bars reflect two standard deviations from the mean value in the integration period. Grey dashed lines indicate the age components as found from the single spot ablations. Steps increase from left (half grain thickness) to right (grain edge).

Table 2
Whole rock compositions for sample 205 used in phase equilibria modelling.

weight %												
SiO_2	TiO_2	Al_2O_3	Fe_2O_3	MgO	MnO	CaO	Na_2O	K_2O	SrO	BaO	LOI	Total
72.20	0.18	14.90	1.52	0.59	0.02	2.09	4.71	2.52	0.12	0.26	0.27	99.46
mol.%												
SiO_2	TiO_2	Al_2O_3	FeO	MgO	MnO	CaO	Na_2O	K_2O	O			H_2O
78.81	0.15	9.59	1.25	0.96	–	2.45	4.98	1.75	0.06			+

'+' in excess, '–' not considered

A). However, such profile is modified by later compositionally distinct apatite growth. Other examples of U-Pbcore-rim apatite profiles that imply thermally activated Pb diffusion significantly after apatite crystallization have been recognised from the Archean Akilia Island in Greenland (Chew et al., 2014). Whitehouse et al. (2009) and Sano et al. (1999) also published on this Akilia apatite and concluded it likely recorded both resetting of older apatite and new growth in the Proterozoic.

5.2.2. Metamorphic apatite growth

The c. 2500 Ma age of apatite in the leucosome bearing tonalitic gneiss (sample 216) is interpreted to reflect the time of apatite growth during metamorphism, consistent with a comparable zircon crystallization age of 2558 ± 8 Ma for a late cross-cutting granite sheet (sample 215) that intrudes these gneisses. Neither, BSE or CL imaging reveals any significant zonation nor overgrowths in sample 216 apatite, which is generally sub- to euhedral. The apparent lack of clear overgrowths in the imaging can be explained by the magnitude of compositional difference, especially in U, which is much less than in sample 205 apatite which does display rims (the U content in apatite 216 rims is twice thatin cores, whereas apatite 205 rims U is at least five times core concentration).

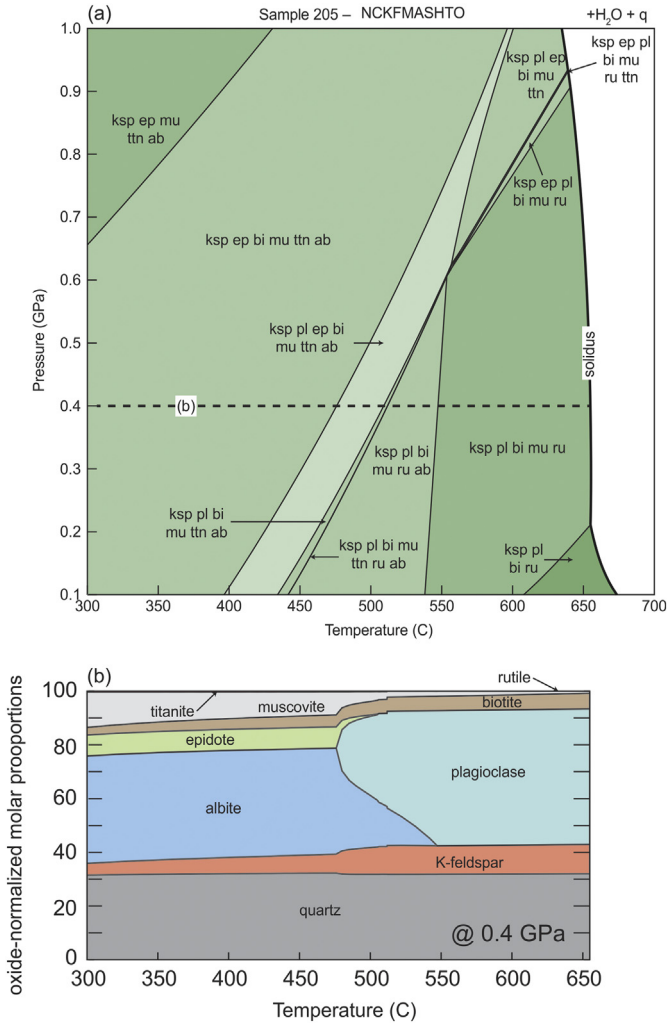

Fig. 7. (a)*P–T* pseudosection for sample 205 in an H_2O-saturated system. Quartz is predicted to be present in all fields. The stability of epidote is restricted to <650°C at ~0.9 GPa and to <450°C at 0.1 GPa. (b)isobaric (0.4 GPa) proportion–temperature diagram illustrating the main mineralogical changes from 300 to 650°C. At 450–500°C, plagioclase is predicted to completely break down to epidote and albite and K-feldspar is expected to partially breakdown to muscovite.

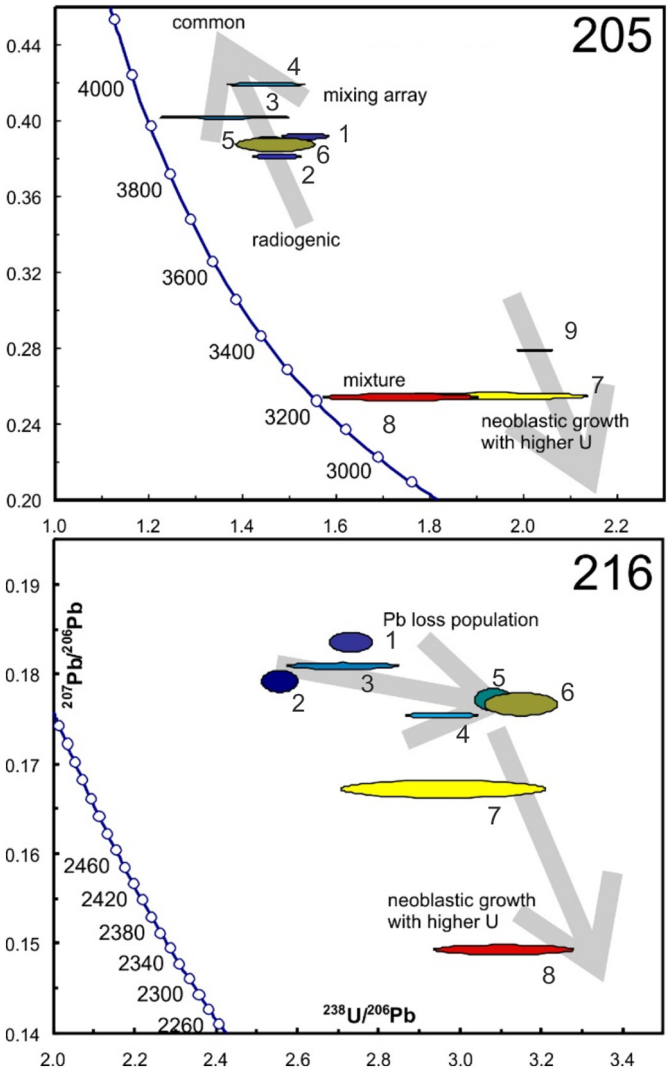

Fig. 8. Inverse Concordia plots for depth profile ablations colours are coded according to integration step with warmer colours indicating a higher step and thus position closer to grain rim. Grey arrows denote interpreted response of U/Pb isotopic system to stated process.

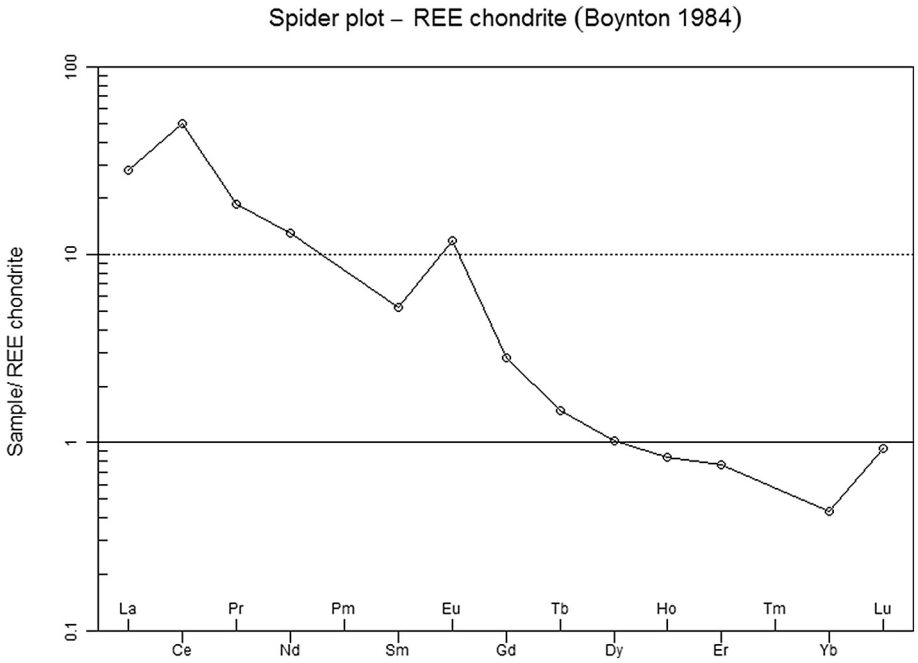

Fig. 9. Bulk rock REE plot for sample 205. Note the positive Eu anomaly.

5.2.3. Apatite dissolution and regrowth

The younger apparent apatite ages of c. 2150 Ma in sample 205, associated both with lower Mn content and lower La_N/Sm_N ratios, imply the growth of a new metasomatic apatite phase later in the history of this rock. Metamorphic apatites are commonly characterized by depletion of Th and LREE, particularly in metapelitic samples where apatite coexists with monazite (Spear and Pyle, 2002). The lower La_N/Sm_Nratios in the c. 2150 Ma apatite component, from the discrete grain analysis, therefore could imply competition from monazite during later apatite growth (Henrichs et al., 2018). However, the elevated Th content in the depth profile rims indicates that at least the outermost rims did not grow with monazite, nor has monazite been identifed by mineral liberation analysis in this sample. The upper intercept is similar for both generations of apatite implying a process in which there was no U-rich mineral breakdown in the rock along with new mineral growth, to result in a different common Pb composition. The CL images of sample 205 apatite (Fig. 2) indicate overgrowths, which are not observable in BSE images. The overgrowth may have been generated during a dissolution regrowth process because the inner part appears slightly embayed. To account for the small amount of epidote observed in the sample, dissolution–reprecipitation in response to an infiltrating fluid must have occurred at $T < 600$ °C (Fig. 7), which is around the closure temperature for Pb in apatite.

The younger U-Pb regression from sample 216 apatite of c. 1800 Ma is interpreted to reflect new apatite growth from a compositionally distinct reservoir (Fig. 8) driven by regional tectonothermal and fluid activity, consistent with c. 1800 Ma phlogopite Ar-Ar ages in ultramafic complexes in the region (Cruz et al., 2016). Those analyses defining the younger regression have, on average, lower Sr, U and total REE than the older apatite population and apparently a different common Pb composition. The mobility of Sr and U is well known in hydrothermal solutions (Cherniak and Ryerson, 1993; Piccoli and Candela, 2002; Sha and Chappell, 1999) and REEs may be incorporated into or removed from apatite via coupled substitution reactions (Hughes and Rakovan, 2015). Additionally, grain depth profiling points to the growth of new U and Th rich apatite during the same process as causing recrystallization of c. 2500 Ma metamorphic apatite. Hence, there appears to be strong temporal coupling between loss of Pb in cores and the growth of REE,U and Th enriched apatite rims.

5.3. Apatite grain size and apparent age

Fig. 10 presents probability density plots of ^{207}Pb corrected apparent age versus grain size for both apatite samples. Radiogenic-Pb loss has been shown in some apatite systems to be solely, or at least dominantly, a function of thermally activated diffusion (Blackburn et al., 2011), a key requirement to use the mineral in thermochronometry modelling. In a situation of thermally activated volume diffusion it would be expected to observe distinct grain size populations that correspond to grain age populations; for example, a larger grain size population would correspond to an older age component, whereas a smaller grain size component may relate to a younger age component given Pb-in-apatite diffusion and spherical geometry characteristics (Cherniak, 2005; Cherniak et al., 1991). The histograms of grain age all indicate bimodal distributions whereas the grain size distributions are multimodal. Moreover, a significant grain size component in these, and likely many apatite geochronology samples, will not be characterizable given current analytical size constraints. Some authors have cautioned that fluid driven elemental mobility may be important in apatite geochronology and thus thermally activated volume diffusion a secondary process affecting U-Pb dates (Bingen et al., 1996; Chen and Simonetti, 2013; Chew et al., 2011; Chew and Spikings, 2015; Cochrane et al., 2014; Corfu and Stone, 1998). For the Greenland samples investigated in this work, fluid driven disturbance and growth processes are implicated on the basis of grain internal textures, petrography, and the relationship between apparent ages and chemistry, where new rim growth appears to be coeval with core U-Pb resetting.

5.4. Radiogenic-Pb loss and new apatite growth

The Pb diffusion closure temperature for apatite has been investigated by several workers (Cherniak, 2010; Cherniak et al., 1991; Krogstad and Walker, 1994) and Pb closure temperatures of around c.600 °C for large 100–200 mm apatite grains have been suggested (Krogstad and Walker, 1994). However other studies, comparing dates from different isotopic systems, have implied a somewhat lower closure temperature of c. 400–500 °C for apatite that may more generally apply (Chamberlain and Bowring, 2001). Apatite in both samples are associated with biotite and are located in fractured regions where fluids may

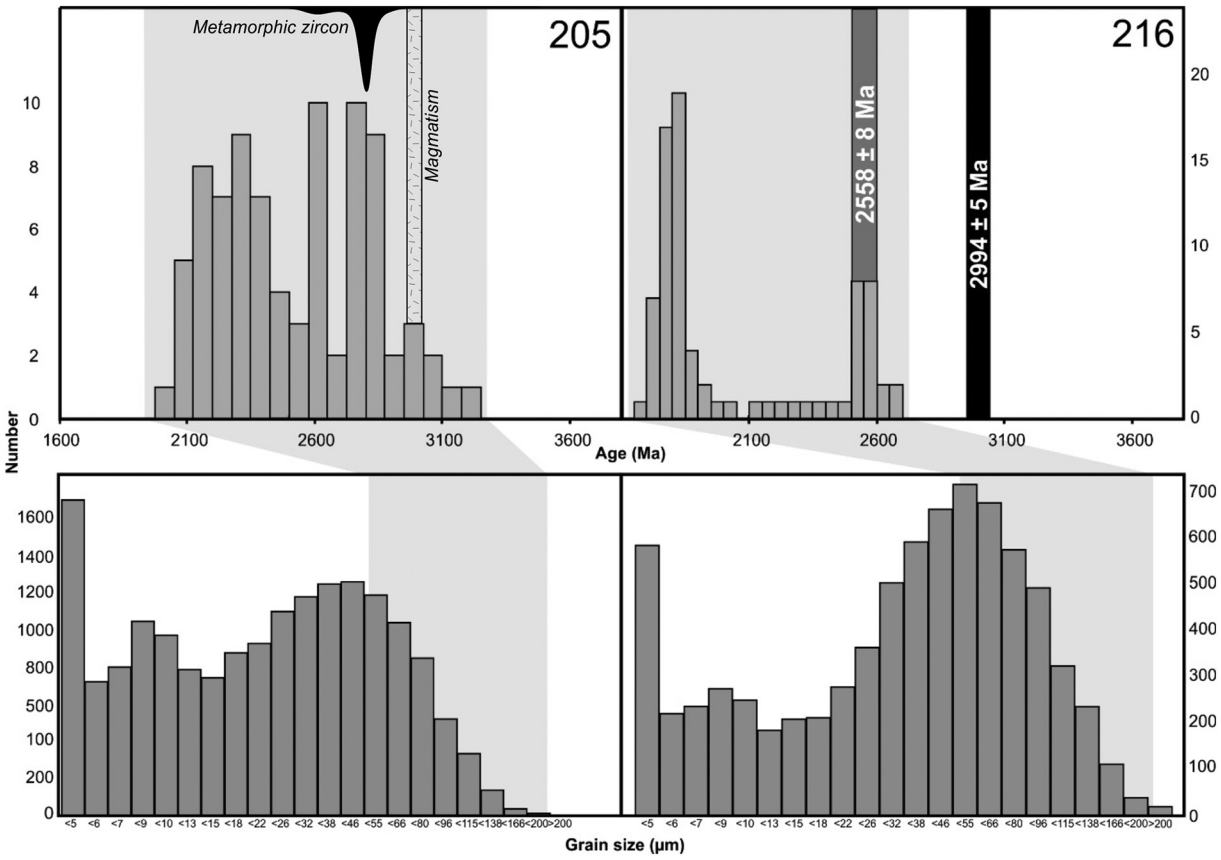

Fig. 10. Histograms of apatite grain size (bottom) versus apparent age (top). The grey field denotes the grain size range that is accessible to laser beam geochronology. Stippled bar in sample 205 is the regional magmatic crystallization age of tonalities in the Akia Terrane. Black probability density plot inset in sample 205 is the age of metamorphic zircon overgrowths in the Akia Terrane (from Kirkland et al., 2018). The black vertical bar in sample 216 is the age of zircon, interpreted to reflect leucosome crystallization. Grey vertical bar is the age of a cross-cutting granite sheet (215) coeval with metamorphic apatite in sample 216. Apatite age in millions of years is the ^{207}corrected age.

have developed. In the current example of Archean apatite from Greenland it is challenging to accept that any of the age-depth profiles reflect solely thermally activated volume diffusion, given that the lower apparent age steps correspond with chemical (and in the case of sample 205) petrographically distinct new rims as well as the relatively low metamorphic temperatures calculated (< 600 °C) during any fluid ingress. The mineral apatite has been considered potentially favourable for investigating post magmatic crystallization thermal histories because of its Pb diffusion temperature, which is lower than many other U-Pb chronometers. Specifically, with knowledge of appropriate diffusion rates and accepting some simplifying assumptions, for example in regard to homogeneity of the diffusion process, it might be considered feasible to invert any age-depth profile in apatite to recover information on the mineral's thermal pathway. However, recrystallization or dissolution-regrowth would render any such thermal history from age-depth profiles suspect, as the patterns would not be governed by Pb diffusion alone.

6. Conclusions

1. Individual apatite generations (discrete grains or overgrowths) may incorporate different common Pb based on their local (microscopic) environment, which could be important for understanding neoblastic versus cooling ages given the high ratio of common to radiogenic Pb in some apatite grains.
2. Chemical and age zoning can be present in apatite even where apparently difficult to resolve in CL and BSE imaging. This age and chemical zonation need not directly spatially correspond, due to different diffusion rates.
3. New apatite rim growth may be coeval with recrystallization and dissolution of older cores.
4. These dissolution/regrowth features in apatite can be formed at temperatures close to the lower temperature limits of what is generally thought to be the closure temperature of Pb diffusion in this mineral.
5. To apply Pb diffusion profiles to determine cooling histories, one must not assume but demonstrate that thermally activated volume diffusion is justifiable because our results show that apatite generally may not record simple thermally activated Pb diffusion profiles but rather profiles modified in part or whole by recrystallization or new growth.
6. Dissolution and regrowth forming high U rims is prevalent in these Greenland apatite and further illustrates this mineral is highly useful in tracking the timing of <600 °C fluid-rock interaction.

Acknowledgments

Two anonymous reviewers are sincerely thanked for comments that have improved this work. The Ministry of Mineral Resources (MMR) of the Greenland Government is acknowledged for supporting the field and analytical work in the Maniitsoq region, SW Greenland.

Appendix A. Supplementary data

Supplementary data to this article can be found online at https://doi.org/10.1016/j.lithos.2018.08.007.

References

Bingen, B., Demaiffe, D., Hertogen, J., 1996. Redistribution of rare earth elements, thorium, and uranium over accessory minerals in the course of amphibolite to granulite facies

metamorphism: the role of apatite and monazite in orthogneisses from southwestern Norway. Geochim. Cosmochim. Acta 60, 1341–1354.
Blackburn, T., Bowring, S.A., Schoene, B., Mahan, K., Dudas, F., 2011. U-Pb thermochronology: creating a temporal record of lithosphere thermal evolution. Contrib. Mineral. Petrol. 162, 479–500.
Black, L.P., Kamo, S.L., Allen, C.M., Davis, D.W., Aleinikoff, J.N., Valley, J.W., Mundil, R., Campbell, I.H., Korsch, R.J., Williams, I.S., Foudoulis, C., 2004. Improved $^{206}Pb/^{238}U$ microprobe geochronology by the monitoring of a trace-element-related matrix effect: SHRIMP, ID-TIMS, ELA-ICP-MS and oxygen isotope documentation for a series of zircon standards. Chem. Geol. 205, 115–140.
Bridgewater, D., Schiøtte, L., 1991. The Archean gneiss craton of northern Labrador. Areview of current results, ideas and problems. Bull. Geol. Soc. Denmark 39, 133–153.
Chamberlain, K.R., Bowring, S.A., 2001. Apatite-feldsparU-Pb thermochronometer: a reliable mid-range (~450°C), diffusion controlled system. Chem. Geol. 172, 173–200.
Chen, W., Simonetti, A., 2013. In-situ determination of major and trace elements in calcite and apatite, and U-Pb ages of apatite from the Oka carbonatite complex: insights into a complex crystallization history. Chem. Geol. 353, 151–172.
Cherniak, D.J., 2000. Rare earth element diffusion in apatite. Geochim. Cosmochim. Acta 64, 3871–3885.
Cherniak, D.J., 2005. Uranium and manganese diffusion in apatite. Chem. Geol. 219, 297–308.
Cherniak, D.J., 2010. Diffusion in accessory minerals: zircon, titanite, apatite, monazite and xenotime. Rev. Mineral. Geochem. 827–869.
Cherniak, D.J., Ryerson, F.J., 1993. A study of strontium diffusion in apatite using Rutherford backscattering spectroscopy and ion implantation. Geochim. Cosmochim. Acta 57, 4653–4662.
Cherniak, D.J., Lanford, W.A., Ryerson, F.J., 1991. Lead diffusion in apatite and zircon using ion implantation and Rutherford Backscattering techniques. Geochim. Cosmochim. Acta 55, 1663–1673.
Chew, D.M., Donelick, R.A., 2012. Combined apatite fission track and U-Pb dating by LA-ICP-MS and its application in apatite provenance analysis. Quant. Mineral. Microanal. Sediment. Sediment. Rocks 42, 219–247.
Chew, D.M., Spikings, R.A., 2015. Geochronology and thermochronology using apatite: time and temperature, lower crust to surface. Elements 11, 189–194.
Chew, D.M., Sylvester, P.J., Tubrett, M.N., 2011. U-Pb and Th-Pb dating of apatite by LA-ICPMS. Chem. Geol. 280, 200–216.
Chew, D.M., Petrus, J.A., Kamber, B.S., 2014. U-PbLA-ICPMS dating using accessory minerals standards with variable common Pb. Chem. Geol. 363, 185–199.
Chu, M.F., Wang, K.L., Griffin, W.L., Chung, S.L., O'Reilly, S.Y., Pearson, N.J., Iizuka, Y., 2009. Apatite composition: tracing petrogenetic processes in Transhimalayan granitoids. J. Petrol. 50, 1829–1855.
Cochrane, R., Spikings, R.A., Chew, D., Wotzlaw, J.F., Chiaradia, M., Tyrrell, S., Schaltegger, U., Van der Lelij, R., 2014. High temperature (>350°C) thermochronology and mechanisms of Pb loss in apatite. Geochim. Cosmochim. Acta 127, 39–56.
Corfu, F., Stone, D., 1998. The significance of titanite and apatite U-Pb ages: constraints for the post-magmaticthermal-hydrothermal evolution of a batholithic complex, Berens River area, northwestern Superior Province, Canada. Geochim. Cosmochim. Acta 62, 2979–2995.
Cruz, M., Grove, M., Szilas, K., 2016. Relative diffusion of argon and calcium in Mica and implications for K-Ca dating methods. American Geophysical Union Conference, SanFrancisco. Abstract V33A-3117.
Dodson, M.H., 1973. Closure temperature in cooling geochronological and petrological systems. Contrib. Mineral. Petrol. 40, 259–274.
Fleet, M.E., Pan, Y., 1997. Site preference of rare earth elements in fluorapatite: binary (LREE+HREE)-substituted crystals. Am. Mineral. 82, 870–877.
Friend, C.R.L., Nutman, A.P., 2005. New pieces to the Archean terrane jigsaw puzzle in the Nuuk region, southern West Greenland: steps in transforming a simple insight into a complex regional tectonothermal model. J. Geol. Soc. 162, 147–162.
Friend, C.R.L., Nutman, A.P., Baadsgaard, H., Kinny, P.D., McGregor, V.R., 1996. Timing of late Archean terrane assembly, crustal thickening and granite emplacement in the Nuuk region, southern West Greenland. Earth Planet. Sci. Lett. 142, 353–365.
Garde, A.A., 1990. Thermal granulite-facies metamorphism with diffuse retro-gression in Archean orthogneisses, Fiskefjord, southern West Greenland. J. Metamorph. Geol. 8, 663–682.
Garde, A.A., 1997. Accretion and evolution of an Archean high-grade grey gneiss–amphibolitecomplex: the Fiskefjord area, southern West Greenland. Geol. Greenland Surv. Bull. 177, 115.
Garde, A.A., 2007. A mid-Archean island arc complex in the eastern Akia terrane, Godthåbsfjord, southern West Greenland. J. Geol. Soc. 164, 565–579.
Garde, A.A., Friend, C.R.L., Nutman, A.R., Marker, M., 2000. Rapid maturation and stabilisation of middle Archean continental crust: the Akia terrane, southern West Greenland. Bull. Geol. Soc. Den. 47, 1–27.
Garde, A.A., Dyck, B., Esbensen, K.H., Johansson, L., Möller, C., 2014. The Finnefjeld domain, Maniitsoq structure, West Greenland: differential rheological features and mechanical homogenisation in response to impacting? Precambrian Res. 255, 791–808.
Gawęda, A., Szopa, K., Chew, D., 2014. LA-ICP-MS U-Pb dating and REE patterns of apatite from the Tatra Mountains, Poland as a monitor of the regional tectonomagmatic activity. Geochronometria 41, 306–314.
Glorie, S., Alexandrov, I., Nixon, A., Jepson, G., Gillespie, J., Jahn, B.M., 2017. Thermal and exhumation history of Sakhalin Island (Russia) constrained by apatite U-Pb and fission track thermochronology. J. Asian Earth Sci. 143, 326–342.
Green, E.C.R., White, R.W., Diener, J.F.A., Powell, R., Holland, T.J.B., Palin, R.M., 2016. Activity–composition relations for the calculation of partial melting equilibria in metabasic rocks. J. Metamorph. Geol. 34, 845–869.
Harlov, D.E., 2015. Apatite: a fingerprint for metasomatic processes. Elements 11, 171–176.
Henrichs, I.A., O'Sullivan, G., Chew, D.M., Mark, C., Babechuk, M.G., McKenna, C., Emo, R., 2018. The trace element and U-Pb systematics of metamorphic apatite. Chem. Geol. 483, 218–238.
Holland, T.J.B., Powell, R., 2011. An improved and extended internally consistent thermodynamic dataset for phases of petrological interest, involving a new equation of state for solids. J. Metamorph. Geol. 29, 333–383.
Hughes, J.M., Rakovan, J.F., 2015. Structurally robust, chemically diverse: apatite and apatite supergroup minerals. Elements 11, 165–170.
Jackson, S., Pearson, N.J., Griffin, W.L., Belousova, E.A., 2004. The application of laser ablation - inductively coupled plasma - mass spectrometry to in situ U-Pb zircon geochronology. Chem. Geol. 211, 47–69.
Keulen, N., Garde, A.A., Jørgart, T., 2014. Shock melting of K-feldspar and interlacing with cataclastically deformed plagioclase in granitic rocks at Toqqusap Nunaa, southern West Greenland: implications for the genesis of the Maniitsoq structure. Tectonophysics 662, 328–344.
Kirkland, C.L., Hollis, J., Danišík, M., Petersen, J., Evans, N.J., McDonald, B.J., 2017. Apatite and titanite from the Karrat group, Greenland; implications for charting the thermal evolution of crust from the U-Pb geochronology of common Pb bearing phases. Precambrian Res. 300, 107–120.
Kirkland, C.L., Yakymchuk, C., Hollis, J., Heide-Jørgensen, H., Danišík, M., 2018. Mesoarchean exhumation of the Akia terrane and a common Neoarchean tectonothermal history for West Greenland. Precambrian Res. 314, 129–144.
Krenn, E., Finger, F., 2004. Metamorphic formation of Sr-apatite and Sr-bearing monazite in a high-pressure rock from the Bohemian Massif. Am. Mineral. 89, 1323–1329.
Krogstad, E.J., Walker, R.J., 1994. High closure temperatures of the U-Pb system in large apatites from the Tin Mountain pegmatite, Black Hills, South Dakota, USA. Geochim. Cosmochim. Acta 58, 3845–3853.
Laflamme, C., McFarlane, C.R.M., Fisher, C.M., Kirkland, C.L., 2017. Multi-mineral geochronology: insights into crustal behaviour during exhumation of an orogenic root. Contrib. Mineral. Petrol. 172.
Mao, M., Rukhlov, A.S., Rowins, S.M., Spence, J., Coogan, L.A., 2016. Apatite trace element compositions: a robust new tool for mineral exploration. Econ. Geol. 111, 1187–1222.
Mark, C., Cogne, N., Chew, D., 2016. Tracking exhumation and drainage divide migration of the Western Alps: a test of apatite U-Pb thermochronometer as a detrital provenace tool. Geol. Soc. Am. Bull. 128, 1439–1460.
McDowell, F.W., McIntosh, W.C., Farley, K.A., 2005. A precise ^{40}Ar-^{39}Ar reference age for the Durango apatite (U-Th)/He and fission-track dating standard. Chem. Geol. 214, 249–263.
Nutman, A.P., 2007. Apatite recrystallisation during prograde metamorphism, Cooma, Southeast Australia: implications for using an apatite-graphite association as a biotracer in ancient metasedimentary rocks. Aust. J. Earth Sci. 54, 1023–1032.
Palin, R.M., Weller, O.M., Waters, D.J., Dyck, B., 2016. Quantifying geological uncertainty in metamorphic phase equilibria modelling; a Monte Carlo assessment and implications for tectonic interpretations. Geosci. Front. 7, 591–607.
Paton, C., Woodhead, J.D., Hellstrom, J.C., Hergt, J.M., Greig, A., Maas, R., 2010. Improved laser ablation U-Pb zircon geochronology through robust downhole fractionation correction. Geochem. Geophys. Geosyst. 11.
Paton, C., Hellstrom, J., Paul, B., Woodhead, J., Hergt, J., 2011. Iolite: freeware for the visualisation and processing of mass spectrometric data. J. Anal. At. Spectrom. 26, 2508–2518.
Piccoli, P.M., Candela, P.A., 2002. Apatite in igneous systems. Rev. Mineral. Geochem. 48, 255–292.
Powell, R., Holland, T., Worley, B., 1998. Calculating phase diagrams involving solid solutions via non-linear equations, with examples using THERMOCALC. J. Metamorph. Geol. 16, 577–588.
Sano, Y., Terada, K., Takahasho, Y., Nutman, A.P., 1999. Origin of life from apatite dating? Nature 400127.
Scherstén, A., Garde, A.A., 2013. Complete hydrothermal re-equilibration of zircon in the Maniitsoq structure, West Greenland: a 3001 ma minimum age of impact? Meteorit. Planet. Sci. 48, 1472–1498.
Schmitz, M.D., Bowring, S.A., Ireland, T.R., 2003. Evaluation of Duluth complex anorthositic series (AS3) zircon as a U-Pb geochronological standard: new high-precision isotope dilution thermal ionization mass spectrometry results. Geochim. Cosmochim. Acta 67, 3665–3672.
Schoene, B., Bowring, S.A., 2006. U-Pb systematics of the McClure Mountain syenite: Thermochronological constraints on the age of the 40Ar/39Ar standard MMhb. Contrib. Mineral. Petrol. 151, 615–630.
Schoene, B., Bowring, S.A., 2007. Determining accurate temperature–time paths from U–Pb thermochronology: an example from the Kaapvaal craton, southern Africa. Geochim. Cosmochim. Acta 71, 165–185.
Sha, L.K., Chappell, B.W., 1999. Apatite chemical composition, determined by electron microprobe and laser-ablation inductively coupled plasma mass spectrometry, as a probe into granite petrogenesis. Geochim. Cosmochim. Acta 63, 3861–3881.
Sláma, J., Košler, J., Condon, D.J., Crowley, J.L., Gerdes, A., Hanchar, J.M., Whitehouse, M.J., 2008. Plešovice zircon—a new natural reference material for U–Pb and Hf isotopic microanalysis. Chem. Geol. 249, 1–35.
Spear, F.S., Pyle, J.M., 2002. Apatite, monazite, and xenotime in metamorphic rocks. In: Kohn, M.J., Rakovan, J., Hughes, J.M. (Eds.), Phosphates: Geochemical, Geobiological, and Materials Importance: Reviews in Mineralogy and Geochemistry. 48. Mineralogical Society of America, Washington, D. C., pp. 293–335.
Stacey, J.S., Kramers, J.D., 1975. Approximation of terrestrial lead isotope evolution by a two-stage model. Earth Planet. Sci. Lett. 26, 207–221.
Stern, R., 2001. A new isotopic and trace-element standard for the ion microprobe: preliminary thermal ionization mass spectrometry (TIMS) U–Pb and electron-microprobe data. Geological Survey of Canada, Radiogenic Age and Isotopic Studies, Report 14, p. 11.

Stern, R., Bodorkos, S., Kamo, S., Hickman, A., Corfu, F., 2009. Measurement of SIMS instrumental mass fractionation of Pb isotopes during zircon dating. Geostand. Geoanal. Res. 33, 145–168.

Szilas, K., Kelemen, P.B., Bernstein, S., 2015. Peridotite enclaves hosted by MesoArchean TTG-suite orthogneisses in the Fiskefjord region of southern West Greenland. GeoResJ 7, 22–34.

Thomson, S.N., Gehrels, G.E., Ruiz, J., Buchwaldt, R., 2012. Routine low-damage apatite U-Pb dating using laser ablation-multicollector- ICPMS. Geochem. Geophys. Geosyst. 13.

Weisberg, W.R., Metcalf, J.R., Flowers, R.M., 2018. Distinguishing slow cooling versus multiphase cooling and heating in zircon and apatite (U-Th)/He datasets: the case of the McClure Mountain syenite standard. Chem. Geol. 485, 90–99.

Whitehouse, M.J., Myers, J.S., Fedo, C.M., 2009. The Akilia controversy: field, structural and geochronological evidence questions interpretations of> 3.8Ga life in SW Greenland. J. Geol. Soc. 166 (2), 335–348.

Wilton, D.H.C., 1994. Metallogenic overview of the Nain Province, northern Labrador. Can. Inst. Mining Metal. Petrol. Bull. 89, 43–52.

Wingate, M.T.D., Kirkland, C.L., 2015. Introduction to geochronology information released in 2015: Geological Survey of Western Australia. 5p. http://geodownloads.dmp.wa.gov.au/downloads/Geochron/pdfs/Intro_2015.pdf.

Winther, K.T., Newton, R.C., 1991. Experimental melting of hydrous low-K tholeiite: evidence on the origin of Archean cratons. Bull. Geol. Soc. Den. 39.